ChemComm
Chemical Communications

Accepted Manuscript

This article can be cited before page numbers have been issued, to do this please use: Q. Li, L. Wang, X. Ai, H. Chen, J. Zou, G. Li and X. Zou, *Chem. Commun.*, 2020, DOI: 10.1039/D0CC06072K.

ROYAL SOCIETY OF CHEMISTRY

rsc.li/chemcomm

Cite this: DOI: 10.1039/c0xx00000x

www.rsc.org/xxxxxx

ARTICLE TYPE

Multiple crystal phases of intermetallic tungsten borides and phase-dependent electrocatalytic property for hydrogen evolution

Qiuju Li,‡ Lina Wang,‡ Xuan Ai, Hui Chen, Jiayun Zou, Guo-Dong Li* and Xiaoxin Zou*

Received (in XXX, XXX) Xth XXXXXXXXX 20XX, Accepted Xth XXXXXXXXX 20XX
DOI: 10.1039/b000000x

Four stoichiometric W-B intermetallic phases, including W_2B, WB, WB_2 and WB_3, are synthesized, and their hydrogen-evolution electrocatalytic properties and electronic structures are investigated comparatively. The electrocatalytic activity for the hydrogen evolution reaction is found to first increase from W_2B to WB_2 and then decrease; and this activity trend can be rationalized based on their different degree of hybridization between *d* orbitals of W and *sp* orbitals of B.

Intermetallic borides are a class of important functional inorganic solids that cover a wide range of constituent metals, compositions and crystal structures.[1-4] Some of them exhibit exceptional bulk properties, including permanent magnetism, thermoelectricity, superhardness and superconductivity.[5-8] These outstanding bulk properties of intermetallic borides are generally attributed to the unique crystal structures in which ionic, covalent and metallic bonding types coexist, as well as the tunable *d-sp* orbital hybridization between metals and boron atoms. The multiple types of bonding and the metal-boron interplay also endow intermetallic borides with some exciting surface catalytic functions (*e.g.*, electrocatalytic water splitting and N_2 fixation as well as catalytic hydrogenation),[1, 9-13] but the relevant studies emerged relatively recently. The main bottleneck restricting the development of boride catalysts lies in the lack of enough knowledge about synthetic chemistry, surface adsorption and electronic properties as well as structure-bonding-function correlations of intermetallic borides.

In this context, several synthetic methods without using high pressures have been developed to access intermetallic borides that are compatible with the needs of catalysis studies.[10, 14-17] But progress is not easy, because precision synthesis of pure and/or metastable crystal phases of intermetallic borides is still challenging. Success has been limited to the synthesis of either a small group of intermetallic borides with a fixed stoichiometry (*e.g.*, T_M:B = 1:2; T_M = transition metal)[16-18] or multiple crystal phases of a few of transition metal-boron systems (*e.g.*, Ru-B system).[19, 20] For instance, a family of transition metal diborides comprising group IVB-VIII metals were synthesized by our group based on borothermic reduction reaction or quasi solid-state metathesis reaction, and their trend in electrocatalytic activity for the hydrogen evolution reaction (HER) was investigated experimentally and theoretically.[16, 17] Among transition metal diborides, RuB_2 was found to be the most efficient catalyst with Pt-like activity for HER, and WB_2 was identified as the highest active, nonprecious metal material.[16, 17] Our further comparative investigation of multiple crystal phases of intermetallic ruthenium borides revealed that the boat-like covalent boron sheets in RuB_2 were the crucial structural subunits, and their electronic interaction with Ru atoms generated highly efficient hydrogen-evolution electrocatalytic active sites.[19]

W-B intermetallics contain multiple crystal phases with different boron substructures. Considering the unique advantages of nonprecious WB_2,[16, 17] a deeper study on the W-B intermetallics as electrocatalysts for HER is important. However, the study is challenging due to the difficulty in precise synthesis of different W-B intermetallics. In this work, we aim to selectively synthesize multiple crystal phases of intermetallic tungsten borides, and to comparatively investigate their crystal and electronic structures as well as their phase-dependent hydrogen evolution electrocatalytic performances. We also want to reveal the effect of hybridization of W *d* orbitals and B *sp* orbitals on surface catalytic behaviors of intermetallic tungsten borides.

We first compared the crystal structures of four intermetallic tungsten borides including W_2B, WB, WB_2 and WB_3. As the ratio of tungsten to boron increases, the boron substructures in these borides evolve from isolated atoms to 1D chains, and then to 2D networks. W_2B possesses the lowest boron content (Fig. 1a), and the isolated boron atoms is located in the central void of a square antiprism composed of eight tungsten atoms (Fig. S1 in Supplementary Information (SI)). As for WB (Fig. 1b), the B-B distance significantly decreases, and the boron atoms form zig-zag chains which alternate orthogonally. In WB_2 (Fig. 1c), the boron atoms are covalently bonded to form two types of 2D networks, graphene-like boron layers (top of Fig.1e) and puckered boron layers (middle of Fig.1e), which are stacked alternately with tungsten layers. WB_3 (Fig.1d) also contains graphene-like boron layers similar to WB_2 (bottom of Fig.1e). However, the tungsten layers in WB_3 can be viewed as the result of removing one third of tungsten atoms (marked by the blue dotted circles) from close-packed tungsten layers.[21]

In order to better understand the bonding of these four intermetallic tungsten borides, the average distance of adjacent W-W and B-B atoms, as well as electron location function (ELF) were calculated. As shown in Fig. 1f, the B-B distance decreases with the increase of boron content, while the W-W distance increases from W_2B to WB_2. Due to the similar crystal structures, WB_3 possesses a W-W distance close to WB_2. ELF analysis (Fig. 1g and Fig. S2 in SI) reveals that there are relatively large ELF values

View Article Online
DOI: 10.1039/D0CC06072K

(0.8-0.9) between two adjacent B atoms in WB, WB_2 and WB_3, indicating the existence of B-B covalent bond in them. The B-B distance is too long to form B-B bonds in W_2B. The ELF values between W-W atoms are in the range of 0.4 to 0.5, reflecting the formation of W-W metallic bond. Owing to the difference in ELF around adjacent W and B atoms, the W-B bond is ionic. This result is further supported by the Bader charge transfer from W atom to its adjacent B atoms (Table S1 in SI).

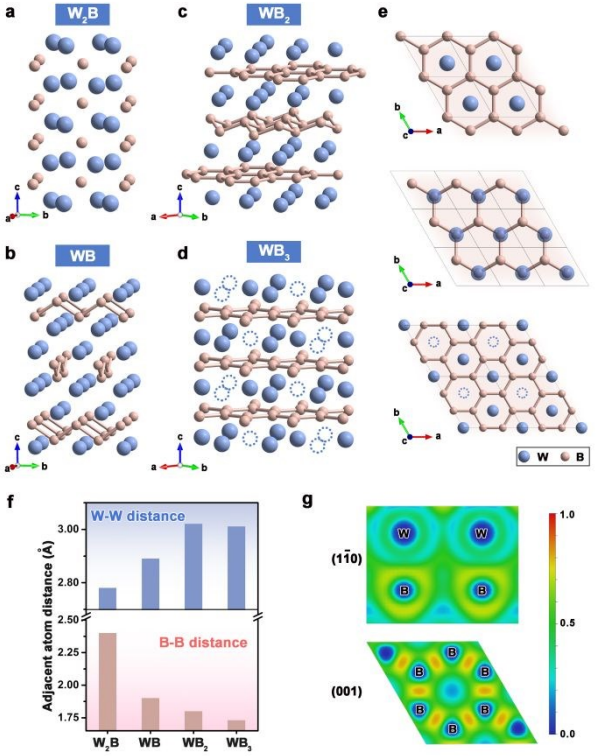

Fig. 1 Crystal structures of (a) W_2B, (b) WB, (c) WB_2 and (d) WB_3. (e) Top view of graphene-like (top) and puckered (middle) boron layers of WB_2, and graphene-like boron layer of WB_3 (bottom). The W atoms deficiency in WB_3 is marked with the blue dotted circle. (f) The average distance of adjacent W-W and B-B atoms of four intermetallic tungsten borides. (g) ELF images of different planes for WB_2.

The interatomic interactions (W-B, W-W and B-B) can also be supported by Crystal Orbital Hamilton Population (COHP) curves. As shown in Fig. 2a and Fig. S3 in SI, the results confirm the metallic W-W and ionic W-B bonding nature in all four intermetallic tungsten borides, as well as the covalent B-B bonding nature in WB, WB_2 and WB_3. Moreover, the integrated COHP (-ICOHP), which is used as a measure of bonding strength, was also analyzed (Fig. 2b and Table S2 in SI). Generally, the larger the -ICOHP value, the stronger the bonding strength. As the boron content increases, the -ICOHP value of W-W decreases, while that of B-B increases. This is contrary to the trends in W-W and B-B distances. The density of states (DOS) and projected density of states (pDOS) of metallic W and intermetallic tungsten borides were calculated and displayed in Fig. 2c. All four intermetallic tungsten borides have metallic properties, with the DOS crossing the Fermi level. In addition, the pDOS reveals that there is the DOS overlap between the W *d* orbitals and the B *sp* orbitals in intermetallic tungsten borides, also suggesting the orbital hybridization between W and B atoms. As a result, intermetallic tungsten borides generally possess broader *d*-bands compared with metallic W.

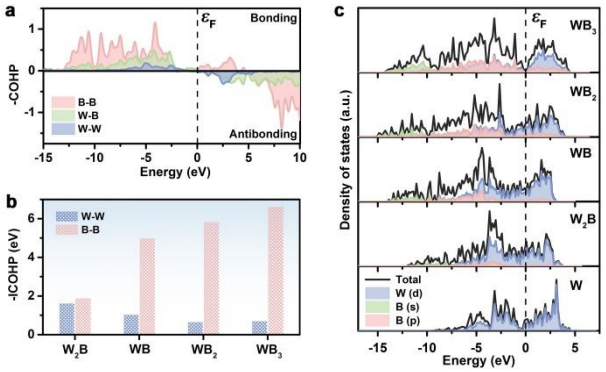

Fig. 2 (a) COHP curves of WB_2. (b) The integrated COHP (-ICOHP) of W_2B, WB, WB_2 and WB_3 for different interactions. (c) Calculated DOS and pDOS of W, W_2B, WB, WB_2 and WB_3.

After investigating the crystal structures and electronic properties of these intermetallic tungsten borides, we considered their thermodynamic stability *via* the formation energies (Table S3 in SI). Fig. S4a (SI) presents the calculated convex hull diagram of the W-B system. The four intermetallic tungsten borides have negative formation energies, indicating that these structures are deemed thermodynamically stable and synthesizable in principle. Among four intermetallic tungsten borides, the formation energy of WB is the smallest, implying that WB is the most stable phase. However, the formation energies of these intermetallic tungsten borides are similar to each other, making their selective synthesis difficult.

We employed WCl_6 as tungsten source, MgB_2 as boron source, and Mg as additive, to selectively synthesize these four intermetallic tungsten borides based on the following three adjustments: (i) the ratio of tungsten source and boron source; (ii) the amount of Mg additive; (iii) the reaction temperature. The details are provided in Experimental Section and Table S4 in the SI. As shown in the powder X-ray diffraction (XRD) patterns (Fig. S4b in SI), the as-synthesized samples are phase-pure intermetallic tungsten borides mentioned above. Transmission electron microscopy (TEM) images show that these intermetallic tungsten borides are composed of nanoparticles ranging in size from 15 to 150 nm (Fig. S4c-f in SI). Scanning electron microscopy-energy dispersive X-ray spectrometry (SEM-EDS) mapping images (Fig. S5 in SI) confirm the uniform distribution of W and B in tungsten borides. Additionally, the Brunauer-Emmett-Teller (BET) surface areas of these intermetallic tungsten borides are in the range of 5.5 to 18.6 $m^2\ g^{-1}$ (Table S5 in SI). The X-ray photoelectron spectroscopy (XPS) spectra show that the strength of W-B bonding enhances with the increase of boron content (Fig. S6 in SI).[22] These results illustrate that we have successfully synthesized multiple crystal phases of intermetallic tungsten borides.

Next, we studied the electrocatalytic activities of these intermetallic tungsten borides toward HER in 0.5 M H_2SO_4 solution (See details in Experimental Section (SI)). For comparison, we also evaluated the activities of metallic W nanoparticles (Figures S7 in SI) and 20 wt% Pt/C under the same testing condition. Fig. 3a shows the polarization curves of four intermetallic tungsten borides, W particles and 20 wt% Pt/C. As the benchmarking HER catalyst, Pt/C has excellent activity and

View Article Online
DOI: 10.1039/D0CC06072K

only needs a low overpotential of 17 mV to reach 10 mA cm_{geo}^{-2}. Meanwhile, intermetallic tungsten borides also show good catalytic activities as nonprecious metal materials. WB_2, WB and W_2B exhibit better activities than metallic W, achieving 10 mA cm_{geo}^{-2} current density at overpotentials of 198, 206 and 259 mV, respectively. WB_3 requires a larger overpotential (328 mV) than W (296 mV) at the current density of 10 mA cm_{geo}^{-2}. To further compare the specific activities of four intermetallic tungsten borides and W, we normalized the measured currents by their electrochemical surface areas (ECSAs, estimated from the value of electrochemical double-layer capacitance, Fig. S8 in SI). As shown in Fig. 3b, the comparison result demonstrates that their specific activities follow the same trend as the activities normalized by geometric area. That is, WB_2 > WB > W_2B > W > WB_3. The activity trend can be further confirmed by electrochemical impedance spectroscopy Nyquist plots (Fig. S9 in SI).

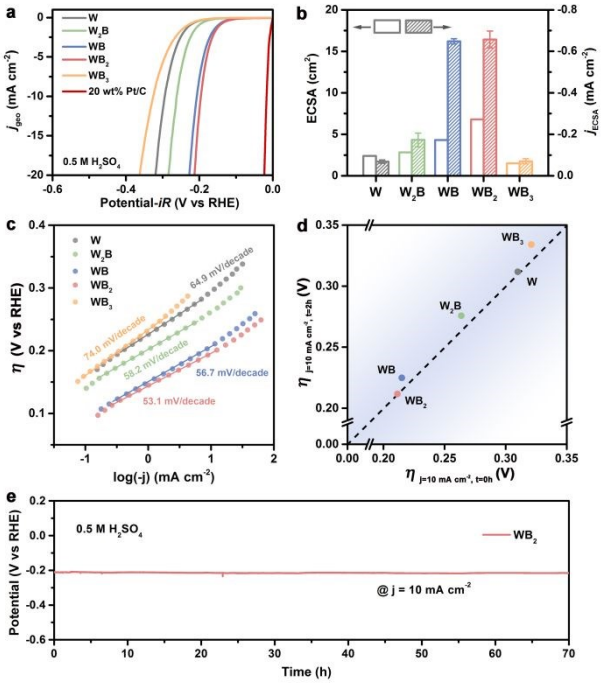

Fig. 3 (a) Polarization curves with 85% *iR*-compensation (the currents were normalized by geometric area of the electrode). (b) Comparison of ECSAs and specific activities (the currents were normalized by ECSAs) at 0.25 V_{RHE}. Error bars indicate standard deviation from five measurements. (c) Tafel plots derived from (a). (d) The short-term stability. The x-axis and y-axis are the overpotentials required to reach 10 mA cm_{goe}^{-2} current density at times t = 0 h and t = 2 h. The dashed line represents the ideal stable catalyst response. (e) Chronopotentiometric curves of WB_2 at 10 mA cm_{goe}^{-2}. All catalysts (including Pt/C, W, W_2B, WB, WB_2 and WB_3) were tested for HER in 0.5 M H_2SO_4 solution.

Additionally, the calculated Tafel plots of the four intermetallic tungsten borides are closed to that of W nanoparticles (Fig. 3c), ranging from 50 to 80 mV $decade^{-1}$. The result indicates that the HER for these intermetallic tungsten borides occurs *via* a Volmer-Heyrovsky mechanism, with electrochemical desorption of hydrogen as the rate-determining step.[23] We evaluated the electrochemical stabilities of intermetallic tungsten borides and metallic W using the chronopotentiometric test. As exhibited in the short-term stability diagram (Fig. 3d), after 2 h of constant polarization, WB_2 and W have no obvious activity loss, whereas the activities of WB, W_2B and WB_3 decrease slightly. Further long-term stability (Fig. 3e) shows that WB_2 can stably electrocatalyze HER in 0.5 M H_2SO_4 solution for at least 70 h, demonstrating its good catalytic stability. WB_2 also exhibits a nearly 100 % Faradaic efficiency (Fig. S11 in SI), indicating a complete electricity-to-hydrogen conversion during HER catalysis. Moreover, intermetallic tungsten borides display medium HER performance in 1 M KOH solution, and the activity trend is consistent with which in acidic media (Fig. S12 in SI).

The hydrogen adsorption free energy (ΔG_{H*}) has been determined as an effective descriptor for HER activity, with a value closer to zero indicating an optimal activity.[24] In order to study the relationship between catalytic activity and crystal phase, we calculated ΔG_{H*} values for the most stable H adsorption sites on W-terminated (001) surfaces of intermetallic tungsten borides (Fig. 4a and Fig. S13, Table S6-S8 in SI). For WB_2, there are two types of W-terminated surfaces, denoted as WB_2-I (Fig. 4b) and WB_2-II (Fig. 4c), whose W layers are bond to graphene-like boron layers and puckered boron layers, respectively. The ΔG_{H*} values for Pt (111) and W (110) surfaces were also included for comparison. The benchmark catalyst Pt holds a near-zero ΔG_{H*} value. Among the four intermetallic tungsten borides, WB_2-I has the smallest absolute ΔG_{H*} values, followed by WB. W_2B exhibits a moderate ΔG_{H*} value similar to W, while the ΔG_{H*} value of WB_3 is far negative than W. Such change trend of ΔG_{H*} value is consistent with that of HER activity observed in the aforementioned experiment.

We noticed a significant difference in ΔG_{H*} values of WB_2-I (-0.40 eV) and WB_2-II (-0.73 eV) surfaces, suggesting that WB_2-I is the catalytic surface with higher HER activity in WB_2. In order to explore the difference in activity of the two catalytic surfaces, we calculated the *d*-band centers of the surface W atoms in the slab models for W, WB_2-I and WB_2-II. As shown in Fig. 4d and Fig. S14 (SI), the *d*-band center of WB_2-I downshifts from -1.02 eV to -1.51 eV compared with that of W, while the *d*-band center of WB_2-II upshifts to -0.91eV. The more negative *d*-band center in WB_2-I means that the antibonding states reduce in energy and become more occupied, resulting in a weaker H adsorption energy and better ΔG_{H*} value.[25] These results, together with the experimental result that WB_2 has the best catalytic activity among four intermetallic tungsten borides, suggest that WB_2-I should be the dominant catalytic surface in WB_2.

We next attributed the variations of *d*-band center to local changes in the adsorption sites, including strain effect and ligand effect. [18, 25] On the one hand, the incorporation of B atoms in W framework causes lattice expansion, which can be demonstrated by the W-W bonding in WB_2 being longer than metallic W (2.76 Å). This tensile strain will reduce the W *d*-orbital overlap and band width, thereby upshifting the *d*-band center (called the strain effect). On the other hand, the orbital hybridization between W and B atoms always results in the broadening of *d*-band width and downshift of *d*-band center (called the ligand effect). Generally, the higher the coordination number, the more negative the *d*-band center. For WB_2-I and WB_2-II surfaces, the B coordination number of surface W atoms is 6 and 4 (insets in Fig.4b and 4c), respectively. This implies that WB_2-I surface has a stronger interatomic *d*-*sp* orbital hybridization than WB_2-II surface, which can be further proved by the -ICOHP values per unit cell (Table S9 in SI). These results indicate that ligand effect has a dominant role

in the modulation of *d*-band structure for WB_2-I, while for WB_2-II strain effect is the main aspect. Therefore, WB_2-I and WB_2-II show different variations of *d*-band center, compared with W surfaces.

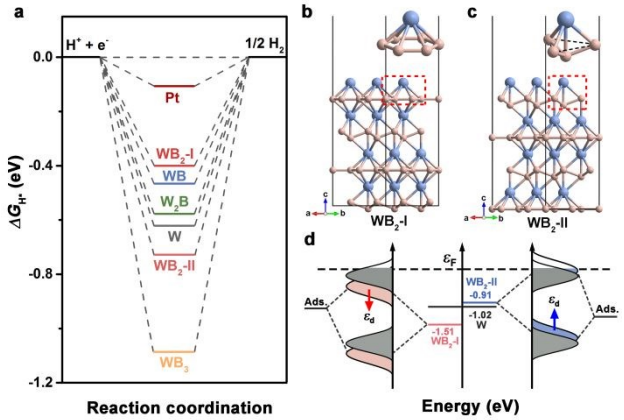

Fig. 4 (a) Calculated ΔG_{H^*} diagram of HER for WB_2-I, WB_2-II, WB_3, WB, W_2B, W and Pt at 100% H^* coverage. Slab models of (b) WB_2-I surface and (c) WB_2-II surface. The insets are partial enlarged views of the corresponding surfaces. (d) The *d*-band centers of the surface W atoms in W, WB_2-I and WB_2-II, as well as schematic explanation for the effect of *d*-band center change on the H adsorption energy.

To reveal how the crystal phase affects the surface catalytic behaviors, we further tried to correlate the *d*-band center (ε_d) with the catalytic activity of intermetallic tungsten borides (Table S10 in SI). However, there is no good consistency. This can be explained by the fact that the *d*-band center is a simple but not precise descriptor, and the *d*-band width (W_d) also affects the interaction energy. Thus, we used a slightly more advanced descriptor, $\varepsilon_d^W = \varepsilon_d + W_d/2$, the upper band-edge energy proposed by Nørskov *at al*.[25] As shown in Table S10 in SI, the upper band-edge energy decreases in the order of: $WB_3 > W_2B > WB > WB_2$-I. Since the upper band-edge energy intrinsically controls the position and occupation of the antibonding states, the upper band-edge energy becomes smaller, and the H adsorption energy (i.e., ΔG_{H^*}) becomes weaker correspondingly. There is a linear correlation between ΔG_{H^*} and upper band-edge energy (Fig. S15 in SI). Besides, the upper band-edge energy correlates with the *d*-band center and *d*-band width, so it is also affected by the combination of strain effect and ligand effect. These results imply that due to the increase of boron content, different crystal phases have different degrees of interatomic *d-sp* orbital hybridization and lattice expansion, thereby will lead to variations of upper band-edge energy and trend of catalytic activities.

In summary, we have synthesized four crystal phases of intermetallic tungsten borides, and investigated their crystal and electronic structures as well as phase-dependent hydrogen evolution activities. We have also demonstrated the influence of interatomic *d-sp* orbital hybridization on catalytic activities in intermetallic tungsten borides. Our results have provided scientific basis for the precise synthesis of other intermetallic borides and the study of boron-regulated catalytic processes for various chemical reactions.

X. Z. thanks the financial supports from the National Natural Science Foundation of China (NSFC) Grant No. 21771079 and 21922507 and the Fok Ying Tung Education Foundation, Grant No. 161011. We also acknowledge NSFC (21975093 and 21621001) and the 111 Project (B17020) for additional financial support. We thank the LvLiang Cloud Computing Center of China, and the calculations were performed on TianHe-2.

Conflicts of interest

There are no conflicts to declare.

Notes and references

State Key Laboratory of Inorganic Synthesis and Preparative Chemistry, College of Chemistry, Jilin University, Changchun 130012, P. R. China; E-mail: xxzou@jlu.edu.cn; lgd@jlu.edu.cn

† Electronic Supplementary Information (ESI) available: [details of any supplementary information available should be included here]. See DOI:10.1039/b000000x/

‡ Q. Li and L. Wang contributed equally to this work.

1. H. Chen and X. Zou, *Inorg. Chem. Front.*, 2020, **7**, 2248-2264.
2. S. Gupta, M. K. Patel, A. Miotello and N. Patel, *Adv. Funct. Mater.*, 2019, **30**, 1906481.
3. S. Carenco, D. Portehault, C. Boissiere, N. Mezailles and C. Sanchez, *Chem. Rev.*, 2013, **113**, 7981-8065.
4. G. Akopov, M. T. Yeung and R. B. Kaner, *Adv. Mater.*, 2017, **29**.
5. H. Tang, X. Gao, J. Zhang, B. Gao, W. Zhou, B. Yan, X. Li, Q. Zhang, S. Peng, D. Huang, L. Zhang, X. Yuan, B. Wan, C. Peng, L. Wu, D. Zhang, H. Liu, L. Gu, F. Gao, T. Irifune, R. Ahuja, H.-K. Mao and H. Gou, *Chem. Mater.*, 2019, **32**, 459-467.
6. R. Mohammadi, C. L. Turner, M. Xie, M. T. Yeung, A. T. Lech, S. H. Tolbert and R. B. Kaner, *Chem. Mater.*, 2016, **28**, 632-637.
7. Y. Shao, M. Shao, Y. Kawazoe, X. Shi and H. Pan, *J. Mater. Chem. A*, 2018, **6**, 10226-10232.
8. T. Mori, *J. Solid State Chem.*, 2019, **275**, 70-82.
9. F. Guo, Y. Wu, H. Chen, Y. Liu, L. Yang, X. Ai and X. Zou, *Energy Environ. Sci.*, 2019, **12**, 684-692.
10. J. Li, H. Chen, Y. Liu, R. Gao and X. Zou, *J. Mater. Chem. A*, 2019, **7**, 5288-5294.
11. X. Liu, Y. Jiao, Y. Zheng and S.-Z. Qiao, *ACS Catal.*, 2020, **10**, 1847-1854.
12. D. Chen, T. Liu, P. Wang, J. Zhao, C. Zhang, R. Cheng, W. Li, P. Ji, Z. Pu and S. Mu, *ACS Energy Lett.,* 2020, **5**, 2909-2915.
13. B.-J. Liaw, C.-H. Chen and Y.-Z. Chen, *Chem. Eng. J.*, 2010, **157**, 140-145.
14. X. Wang, G. Tai, Z. Wu, T. Hu and R. Wang, *J. Mater. Chem. A*, 2017, **5**, 23471-23475.
15. H. Zhang, H. Xiang, F.-z. Dai, Z. Zhang and Y. Zhou, *J. Mater. Sci. Technol.*, 2018, **34**, 2022-2026.
16. Q. Li, X. Zou, X. Ai, H. Chen, L. Sun and X. Zou, *Adv. Energy Mater.*, 2019, **9**, 1803369.
17. F. Guo, Y. Wu, X. Ai, H. Chen, G. D. Li, W. Chen and X. Zou, *Chem. Commun.*, 2019, **55**, 8627-8630.
18. X. Ai, X. Zou, H. Chen, Y. Su, X. Feng, Q. Li, Y. Liu, Y. Zhang and X. Zou, *Angew. Chem. Int. Ed.*, 2020, **59**, 3961-3965.
19. X. Zou, L. Wang, X. Ai, H. Chen and X. Zou, *Chem. Commun.*, 2020, **56**, 3061-3064.
20. E. Lee, H. Park, H. Joo and B. P. T. Fokwa, *Angew. Chem. Int. Ed.*, 2020, **59**, 11774-11778.
21. Q. Tao, D. Zheng, X. Zhao, Y. Chen, Q. Li, Q. Li, C. Wang, T. Cui, Y. Ma, X. Wang and P. Zhu, *Chem. Mater.*, 2014, **26**, 5297-5302.
22. J. Chrzanowska-Giżyńska, P. Denis, S. Woźniacka and Ł. Kurpaska, *Ceram. Int.*, 2018, **44**, 19603-19611.
23. J. O. M. Bockris and E. C. Potter, *J. Electrochem. Soc.*, 1952, **99**, 169.
24. B. Hinnemann, P. G. Moses, J. Bonde, K. P. Jørgensen, J. H. Nielsen, S. Horch, I. Chorkendorff and J. K. Nørskov, *J. Am. Chem. Soc.*, 2005, **127**, 5308.
25. J. K. Nørskov, F. Studt, F. Abild-Pedersen and T. Bligaard, *Fundamental Concepts in Heterogeneous Catalysis*, Wiley, Hoboken, 2014.